



Article

Facile Synthesis of $\text{SnO}_2/\text{LaFeO}_{3-x}\text{N}_x$ Composite: Photocatalytic Activity and Gas Sensing Performance

Xi-Tao Yin ¹, Davoud Dastan ², Fa-Yu Wu ^{1,*} and Jing Li ^{1,*}

¹ The Key Laboratory of Chemical Metallurgy Engineering of Liaoning Province and School of Materials and Metallurgy, University of Science and Technology Liaoning, Anshan 114051, China

² Department of Materials Science and Engineering, Georgia Institute of Technology, Atlanta, GA 30332, USA

* Correspondence: fayuwu@ustl.edu.cn (F.-Y.W.); lijing@ustl.edu.cn (J.L.)

Received: 11 July 2019; Accepted: 9 August 2019; Published: 14 August 2019



Abstract: Here $\text{SnO}_2/\text{LaFeO}_{3-x}\text{N}_x$ composite was fabricated using a wet chemical method and was applied to pollutants degradation and gas sensing for the first time. The composite exhibits high performance for photocatalytic degradation of Rhodamine B (RhB) dye and selectivity sensing of various gases. On the basis of the completed experiments, the improved RhB degradation and selective gas sensing performance resulted from the extended optical absorption via N_2 incorporated surface states and enhanced charge separation via coupling SnO_2 . Using the scavengers trapping experiments, the superoxide radical ($\text{O}_2^{\bullet-}$) was investigated as the major scavenger involved in the degradation of RhB over $\text{SnO}_2/\text{LaFeO}_{3-x}\text{N}_x$ composite. In this paper, the probable reaction steps involved in the RhB dye degradation over $\text{SnO}_2/\text{LaFeO}_{3-x}\text{N}_x$ composite are proposed. This work will provide reasonable strategies to fabricate LaFeO_3 -based proficient and stable catalysts for environmental purification. In addition, the result of the selectivity of gas performance is also presented.

Keywords: $\text{LaFeO}_{3-x}\text{N}_x$; RhB degradation; charge separation; gas sensing

1. Introduction

The degradation of various toxic, organic pollutants via semiconducting nanomaterials with the assistance of solar energy offers a hygienic and environmentally friendly method [1]. However, the detection and monitoring of highly toxic and flammable exhaust gases such as NO_2 , SO_2 , H_2 , and CO are vital for environmental remediation [2–4]. Semiconductor photocatalysts and gas sensors are widely employed for various pollutants oxidation and gas sensing in domestic and industrial surroundings because semiconductor metal oxides are ideal photocatalysts and gas sensors [5–7]. The design of low-cost, robust, and low-power-consuming semiconductor photocatalysts and gas sensors have attracted increasing attention due to their wide range of applications [8,9]. Research has focused on finding appropriate semiconducting nanomaterials with vital surface and bulk properties for high activity, sensitivity, and selectivity [10,11]. Among various metal oxide semiconductors, perovskite-type oxides have been given tremendous attention owing to their prospective applications in advanced technologies like chemical sensors, catalysts, solid oxide fuel cells, and magnetic materials [12]. The Lanthanum Ferrite (LaFeO_3) perovskite ($E_g = 2.0\text{--}2.8$ eV) has been widely utilized in photocatalysis and gas sensing [13,14]. Yet, the performance of bare LaFeO_3 is not sufficient for efficient photocatalysis and gas sensing owing to the short lifetime of photo-induced charge carriers [15]. To improve its performance, doping elements and heterojunctions with other semiconductors are widely used [16,17]. SnO_2 is widely accepted as the best choice for gas sensing and pollutants degradation. Doping elements can greatly alter the surface states of nanomaterials, and coupling metal oxides can enhance charge separation thereby enhancing its performance for photocatalytic and gas sensing applications [18]. Thus, the unique characteristics of heterojunctions can improve the photocatalytic and gas sensing

performance by promoting the charge carrier's separation and transfer. For example, Zhang et al. [19] reported the synthesis of novel A- or B-site substituted LaFeO₃/silica fiber (SF) composite photocatalysts that showed improved photocatalytic performance for degradation of Methylene blue (MB) dye under visible light irradiation. This enhanced activity was attributed to the synergistic effect caused by the doping which introduced surface states and the coupled silica fiber. Recently, Xu et al. [20] reported LaFeO₃/g-C₃N₄ heterojunctions that showed enhanced activities for H₂ evolution and MB degradation under visible light irradiation; these features were attributed to the remarkably enhanced charge carriers separation and transfer by the synergetic effect at the interface of the two components system. According to Armstrong et al. [21], LaFeO₃ exhibits high adsorption capacity for NO_x surface conversion in comparison with the LaMnO₃. This difference was ascribed to the different B-site cations (Fe³⁺) in LaFeO₃ when compared with the LaMnO₃ with Mn³⁺ and Mn⁴⁺ valence states. Toan et al. [22] demonstrated that LaFeO₃ films exhibit high sensitivity for sensing of different concentrations of CO, CH₄, and NO₂ gases in air atmosphere at various temperatures.

It is significant to explore the role of surface active species such as electron (e⁻), hole (h⁺), hydroxyl radical (•OH), and the superoxide radical (O₂^{•-}) in semiconductor photocatalysis and gas sensing. Primary oxidants (•OH) have no selectivity to organic pollutants. However, the O₂^{•-} radical species generated in the conduction band of semiconductors by the interaction of electron with the adsorbed O₂ can oxidize a variety of organic pollutants including dioxins, pesticides, and chlorinated pollutants. The mechanisms of pollutant degradation are strongly influenced by various catalysts and the model pollutants because the designed photocatalyst and the dominant active species decide the degradation mechanism [23,24]. However, the reaction mechanisms of pollutant degradation and gas sensing over a LaFeO₃ semiconductor is not fully understood. Thus, it is necessary to develop a clear mechanism for pollutant degradation and gas sensing over a LaFeO₃ semiconductor. To date, no works related to the fabrication of SnO₂ coupled LaFeO_{3-x}N_x catalyst for RhB dye degradation and gas sensing have been reported.

Here, we report the fabrication SnO₂/LaFeO_{3-x}N_x composite for high performance RhB dye degradation and gas sensing. On the basis of completed experiments, results indicate that the improved photocatalytic performance of SnO₂/LaFeO_{3-x}N_x for RhB dye degradation and gas sensing is accredited to the extended visible-light absorption via doping N₂ and superior charge carrier's separation via coupling SnO₂. Further, it is confirmed by scavenger trapping results that O₂^{•-} radical is the main oxidant species involved the degradation of RhB dye over SnO₂/LaFeO_{3-x}N_x composite. This work will trigger the development of LaFeO₃-based high performance photocatalysts and gas sensors for environmental remediation and will help the scientific community to understand the surface chemistry of these processes.

2. Experimental Section

2.1. Synthesis of LaFeO₃ Nanoparticles

LaFeO₃ was fabricated via a sol-gel technique. In the given experiment, equimolar amount (i.e., 0.04 mol) of La(NO₃)₃·6H₂O and Fe(NO₃)₃·9H₂O was dissolved into 25 mL mixture of ethylene glycol (EG) and water (1:1). The solution was magnetically stirred at room temperature for 4 h to obtain a gel. The gel was dried in oven at 100 °C overnight. Finally, the dry powder was kept in a ceramic crucible and annealed at 600 °C (heating rate = 5 °C min⁻¹) in a muffle furnace for 2 h to obtain LaFeO₃. All reagents were purchased from Aladdin Company. (Aladdin Reagent (Shanghai) Co., Ltd., Shanghai, China).

2.2. Synthesis of LaFeO_{3-x}N_x Oxynitride

To prepare LaFeO_{3-x}N_x oxynitride, 2 g of the fabricated LaFeO₃ was taken in a ceramic boat and kept in a quartz reactor. Next, the quartz reactor was carefully sealed and N₂ gas was allowed to pass through a saturated system concentrated with aqueous ammonia solution. The N₂ was used as a

carrier gas for transportation of ammonia vapor into the reactor. The ammonolysis reaction was carried out at 500 °C for 6 h. When room temperature attained, the $\text{LaFeO}_{3-x}\text{N}_x$ oxynitride photocatalyst was collected.

2.3. Fabrication of $\text{SnO}_2/\text{LaFeO}_{3-x}\text{N}_x$ Nanocomposite

To fabricate SnO_2 coupled $\text{LaFeO}_{3-x}\text{N}_x$ oxynitride composite ($\text{SnO}_2/\text{LaFeO}_{3-x}\text{N}_x$), 1 g of $\text{LaFeO}_{3-x}\text{N}_x$ oxynitride catalyst was dispersed into a 50 mL of ethanol and water mixture (1:1). Subsequently, 5% by mass of SnO_2 was added to it. After continuous stirring for 6 h, the mixture was dried in an oven at 80 °C overnight. The powder was finally annealed at 450 °C (N_2 atmosphere) for 2 h to obtain $\text{SnO}_2/\text{LaFeO}_{3-x}\text{N}_x$ composite.

2.4. Characterization

The crystalline morphology of the photocatalysts was examined by an X-ray diffractometer (D8-Advance, Bruker Inc., Karlsruhe, Germany). The UV-visible, diffuse reflectance spectroscopy spectra (UV-vis DRS) were obtained with a Perkin Elmer UV/Vis spectrometer (Lambda-35, PerkinElmer Inc.). The scanning electron microscopy (SEM) micrographs and the energy dispersive spectroscopy (EDS) spectra were obtained with a scanning electron microscope (GeminiSEM-300-7112, Carl Zeiss Inc., Dresden, Germany). The elemental chemical composition was examined by the X-ray photoelectron spectrometer (AXIS-ULTRA DLD-600W, Shimadzu Inc., Kyoto, Japan). The photoluminescence (PL) and fluorescence (FL) spectra were obtained with a spectrofluoro-photometer (FP-6500, Spectroscopic Co. Ltd., Kyoto, Japan) at 325 nm excitation wavelength.

2.5. Photoelectrochemical Measurements

For photoelectrochemical (PEC) experiments, the electrode films were prepared in advance by a doctor-blade procedure using a high temperature 3 m 2380 scotch tape as the spacer. In a typical procedure, 25 mg of each photocatalyst was dispersed in 1 mL of isopropyl alcohol and kept under ultrasonic treatment for 30 min followed by magnetic stirring for 30 min. Then, 25 mg of highly grinded Macrogol-6000 was added to the photocatalyst solution and the ultrasonic treatment was repeated with magnetic stirring for 30 min each. After that, acetylacetone (0.05 mL) was drop wise added to the solution and vigorously stirred for 48 h. Finally, the product was pasted on thoroughly washed, conductive, fluorine-doped, tin-oxide (FTO) glass substrates (10–15 ohm/sq, Xinyan Tech Ltd., Chengdu, China) and sintered at 450 °C (5 °C min^{-1}) for 30 min. The FTO glass substrates were then cut in to 1.0 cm × 3.0 cm pieces containing the film surface area of 1 cm × 1 cm.

2.6. Photoactivity Evaluation

The experiments were performed in a 100 mL volume glass beaker. A 150 W Xe-lamp (GYZ220, CEAULIGHT. Inc., Beijing, China) with cut-off filter (420 nm) was used as the irradiation source. During photocatalytic process, 50 mg of the photocatalyst was taken into 40 mL of RhB-dye solution (10 mg/L) and continuously stirred for 10 min to reach the adsorption equilibrium. The solution was kept under visible-light irradiation for 2 h. After regular intervals of 30 min, an appropriate amount of RhB-dye solution was taken with a syringe and centrifuged to measure its concentration with a Perkin Elmer UV/Vis spectrometer (Lambda-35, PerkinElmer Inc.), at characteristic optical absorption of 553 nm.

2.7. Gas Sensing Evaluation

Sample preparation: A Pt interdigital electrode was coated on the alumina substrate by screen printing. After annealing at 800 °C, the Pt interdigitated electrode was firmly adhered to the alumina substrate. The photocatalyst powder was mixed with a small amount of organic binder. The binder was prepared by stirring terpineol and ethyl cellulose in a ratio of 1 g of ethyl cellulose to 10 mL of

terpineol. Slurry of photocatalyst for preparing a thick film was obtained. The slurry was uniformly coated on an alumina ceramic sheet having a Pt electrode by a screen printing method to prepare a thick film, and the obtained thick film sheet was annealed at 550 °C for 3 h.

Gas Sensitivity Test: The test system consists of a multi-stage gas dilution system, an electric resistance furnace, and an electrochemical workstation (CHI660E, CH Instruments Inc, Shanghai, China). The sample was placed in an electric resistance furnace connected to two electrodes and an external gas sensing recorder. The experiments were performed at 400 °C. Three kinds of gases, H₂, CO, and SO₂, were chosen, and their concentration in air with exposure time was 500 mL/min. The test gas flow rate was 10 mL/min, and the exposure time was 300–600 s. The test system uses an electrochemical workstation with a set voltage of 4 V. To obtain the “I-t” curves of the material, the current-time relationship was used. To obtain an “R-t” curve, the resistance was calculated using Ohm’s law.

3. Results and Discussion

3.1. Structural Morphology and Chemical Composition

The X-ray diffraction (XRD) patterns of the photocatalysts are shown in Figure 1A. The XRD patterns of LaFeO₃ can be assigned to the highly crystalline perovskite-type orthorhombic phase and indexed to the JCPDS No. 37-1493 [25]. The crystallite size were calculated at intense diffraction peak located at 32.19° (hkl = 121) using Debye Scherrer equation ($D_{\text{size}} = K\lambda/\beta\cos\theta$) [26]. The calculated crystallite size of LaFeO₃, LaFeO_{3-x}N_x, and SnO₂/LaFeO_{3-x}N_x were 100, 107, and 108 nm, respectively. Notably, the intense XRD signal of LaFeO_{3-x}N_x is slightly red shifted which is attributable to the partial substitution of oxygen anion (O²⁻, radius = 1.4 Å) with that of the nitrogen ones (N³⁻, radius = 1.5 Å). Accordingly, O²⁻ has higher electro-negativity (3.5) than N³⁻ (3.07). Thus the robust covalent metal-N₂ bonding reduced the energy band gap of LaFeO₃ and extended its optical absorption behavior [27]. When SnO₂ was coupled with LaFeO_{3-x}N_x, the peaks related to SnO₂ also appeared in the composite, suggesting the successful formation of heterojunction. In addition, SnO₂ coupling did not affect the crystalline phase morphology of LaFeO₃. The UV-Visible diffuse reflectance spectra (UV-Vis DRS) were measured to investigate the absorption behavior of the photocatalysts, as shown in Figure 1B. The energy band gaps of LaFeO₃ and LaFeO_{3-x}N_x photocatalysts were estimated to be 2.0 and 1.84 eV, respectively, based on the energy band gap equation $E_g = 1240/\lambda$. Further, the SnO₂ coupling did not affect the energy band gap of LaFeO_{3-x}N_x. The scanning electron microscopy (SEM) micrographs were obtained to examine the morphology of the photocatalysts. Figure 2A reveals that LaFeO₃ nanoparticles have an average crystallite size of about 100 nm and is in accordance with the XRD crystallite size. As seen in Figure 2B, after ammonolysis reaction for 6 h, the morphology of LaFeO₃ was slightly changed and its particle size was enlarged. The SEM micrograph of SnO₂/LaFeO_{3-x}N_x composite, as seen in Figure 2C, shows that the nano-size SnO₂ particles are present on the surface of LaFeO₃ photocatalyst. The energy dispersive spectroscopy (EDS) spectrum of SnO₂/LaFeO_{3-x}N_x composite, as seen in Figure 2D, shows La, Fe, O, N, and Sn elements, which demonstrate that N was successfully integrated into the crystal lattice of LaFeO₃, and SnO₂ was coupled. The X-ray photoelectron spectroscopy (XPS) spectra were obtained to investigate the chemical composition of the photocatalysts. The binding energies were standardized for specimen charging using C1s as the reference (peak position = 285.0 eV) [28]. The XPS survey spectra of LaFeO₃, LaFeO_{3-x}N_x, and SnO₂/LaFeO_{3-x}N_x are shown in Figure 3A. From the high resolution XPS of La3d seen in Figure 3B, the binding energy peaks at 833.5 and 850.4 eV, respectively, corresponds to the La3d_{5/2} and La3d_{3/2} energy levels. Notably, both of the peaks exhibit a satellite peak at a distance of 4.0 eV and the spin-orbital splitting of La3d_{5/2} and La3d_{3/2} is about 16.9 eV. This reveals that La3d exists in +3 oxidation state. As seen in Figure 3C, the high resolution XPS spectra of Fe2p reveals the presence of Fe2p_{3/2} and Fe2p_{1/2} energy levels at 710 and 723.5 eV, respectively. This confirms the existence of Fe2p in +3 oxidation state [29]. As seen in Figure 3D, the high resolution XPS spectra of O1s shows binding

energy peaks at 529.5 and 531.5 eV, respectively, for lattice oxygen (OL, La–O, and Fe–O bonds), and hydroxyl (OH) one [30]. As seen in Figure 3E, the high resolution N1s XPS spectra for $\text{LaFeO}_{3-x}\text{N}_x$ and $\text{SnO}_2/\text{LaFeO}_{3-x}\text{N}_x$ photocatalysts are broad and sited at binding energy of ~ 399 eV [31,32]. As seen in Figure 3F, the high resolution Sn3d XPS spectra display peaks at binding energies of 486.9 and 495.2 eV, respectively, that correspond to the Sn3d_{5/2} and Sn3d_{3/2} energy levels in pure SnO_2 and $\text{SnO}_2/\text{LaFeO}_{3-x}\text{N}_x$ photocatalysts [33]. Thus, it is confirmed that N is successfully integrated into the matrix of LaFeO_3 and SnO_2 is coupled to it.

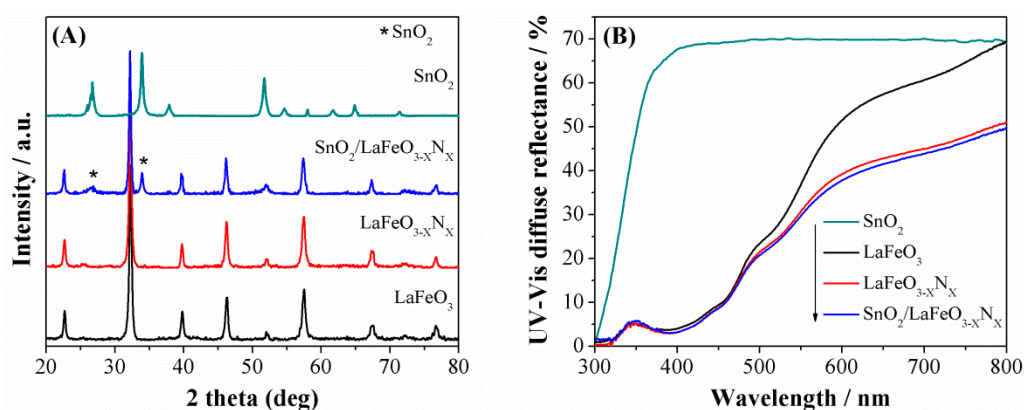


Figure 1. XRD patterns (A) and UV-Visible diffuse reflectance spectra (B) of LaFeO_3 , $\text{LaFeO}_{3-x}\text{N}_x$, $\text{SnO}_2/\text{LaFeO}_{3-x}\text{N}_x$, and SnO_2 photocatalysts.

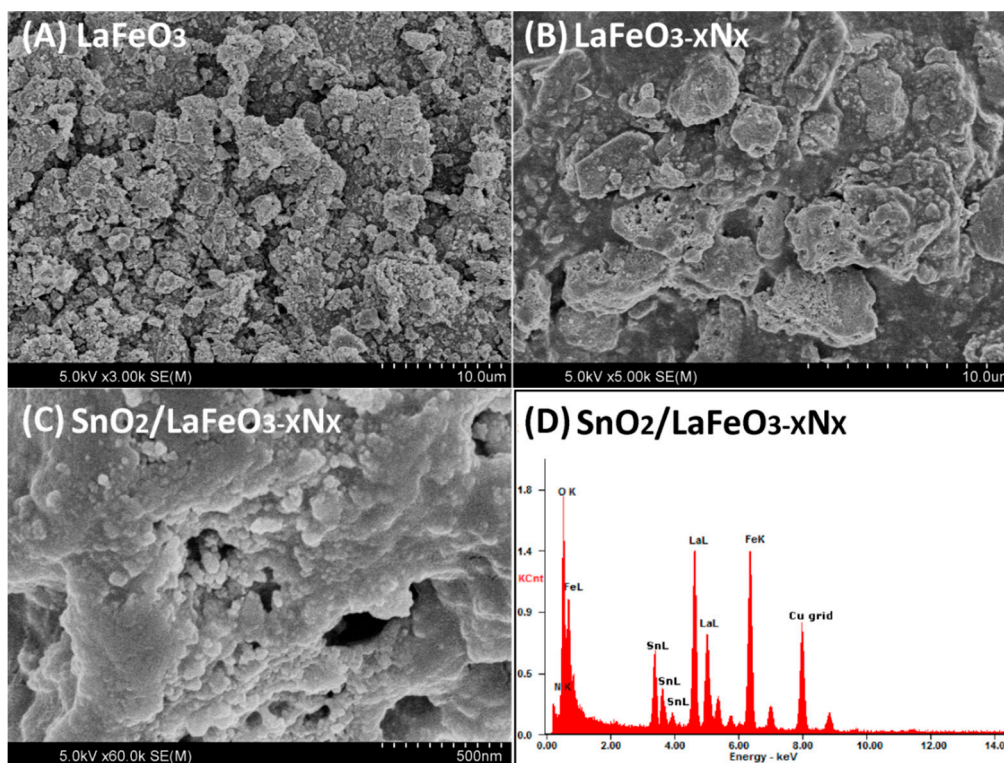


Figure 2. Scanning electron microscopy (SEM) images (A–C) of LaFeO_3 , $\text{LaFeO}_{3-x}\text{N}_x$, and $\text{SnO}_2/\text{LaFeO}_{3-x}\text{N}_x$ photocatalysts, and Energy Dispersive X-ray (EDX) spectrum (D) of $\text{SnO}_2/\text{LaFeO}_{3-x}\text{N}_x$ photocatalyst.

Figure 3. X-ray photoelectron spectroscopy (XPS) survey spectra (A) of LaFeO₃, LaFeO_{3-x}N_x, SnO₂, and SnO₂/LaFeO_{3-x}N_x photocatalysts, high resolution La3d XPS spectra (B) and Fe2p XPS spectra (C) of LaFeO₃, LaFeO_{3-x}N_x, and SnO₂/LaFeO_{3-x}N_x photocatalysts, O1s XPS spectra (D) of LaFeO₃, LaFeO_{3-x}N_x, SnO₂, and SnO₂/LaFeO_{3-x}N_x photocatalysts, N1s XPS spectra with inset valence band XPS spectra of LaFeO₃ and LaFeO_{3-x}N_x (E) and Sn3d XPS spectra (F) of LaFeO_{3-x}N_x and SnO₂/LaFeO_{3-x}N_x photocatalysts.

3.2. Photo-Induced Charge Properties

To inspect the photo-induced charge properties of LaFeO₃, LaFeO_{3-x}N_x, and SnO₂/LaFeO_{3-x}N_x photocatalysts, photoluminescence (PL) spectra were measured. The PL technique is highly sensitive and is used to explore the surface active sites of semiconductor nanomaterials. From PL spectroscopy, we can obtain knowledge regarding defects in semiconductor surfaces, oxygen vacancies, trapping, immigration, and transfer of charges, [34]. As seen in Figure 4A, LaFeO₃ exhibits a strong PL response, which is related to the fast recombination rate of photo-generated charges. Notably, the PL intensity peak of LaFeO_{3-x}N_x is remarkably decreased and further decreased after coupling SnO₂. This demonstrates that the charge carrier's recombination in LaFeO_{3-x}N_x is considerably reduced. To further investigate the enhanced charge carrier's separation, photoelectrochemical (PEC) I-V and I-t curves were measured, as shown in Figure 4B,C. LaFeO₃ exhibits a low photo-current density signal. Notably, the photo-current density signal of LaFeO_{3-x}N_x photocatalyst is obviously improved and that of the SnO₂/LaFeO_{3-x}N_x photocatalyst is significant. The •OH radical can also provide information about the photo-induced charge carrier's separation during semiconductor photocatalysis [35]. The strong fluorescence (FL) signal reflects a large amount of the •OH radical and high charge carrier's separation. Thus, we have detected the •OH amount by the coumarin fluorescent method. In this method, the coumarin react with •OH radical and produce 7-hydroxy-coumarin luminescent species. As shown in Figure 4D, LaFeO₃ photocatalyst produced small amount of •OH radical. However, the amount of •OH radical produced over LaFeO_{3-x}N_x is remarkably increased and significant for the SnO₂/LaFeO_{3-x}N_x nanocomposite. This is in agreement with the PL and PEC results, signifying that charge carrier's separation is remarkably improved.

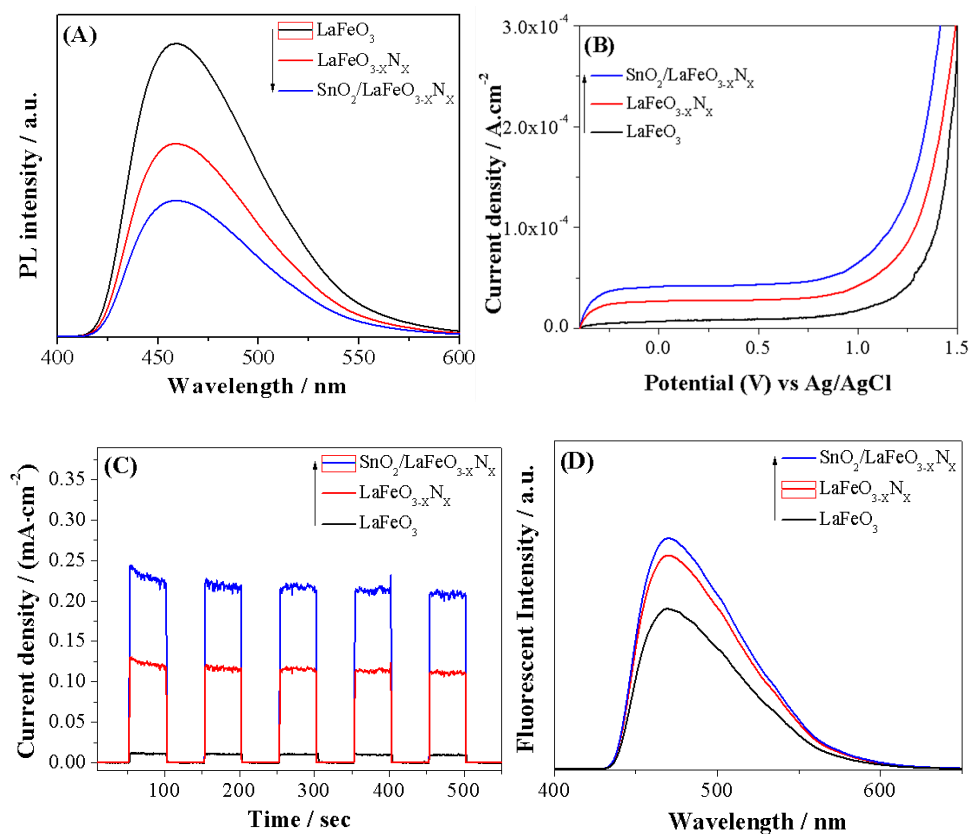


Figure 4. Photoluminescence (PL) spectra (A), photoelectrochemical (PEC) I-V curves (B), PEC I-t curves (C) and fluorescence (FL) spectra (D) of LaFeO₃, LaFeO_{3-x}N_x, and SnO₂/LaFeO_{3-x}N_x photocatalysts.

3.3. Photocatalytic and Gas Sensing Performance

The visible-light activity of the photocatalysts was performed for the RhB-dye degradation and the results are provided in Figure 5A. Notably, LaFeO₃ photocatalyst degraded only 31% of RhB-dye beneath visible-light irradiation for 2 h. The degradation of RhB-dye over LaFeO_{3-x}N_x photocatalyst is considerably high (i.e., 55%). Interestingly, the degradation of RhB-dye over SnO₂/LaFeO_{3-x}N_x composite is significant (i.e., 71%), higher than reported thus far under the same experimental conditions as depicted in Table 1. Notably, the improved photocatalytic activity of LaFeO₃ photocatalyst for RhB-dye degradation is attributed to the extended optical absorption via doping N and to the enhanced charge carrier's separation via coupling SnO₂. Thus, the designed SnO₂/LaFeO_{3-x}N_x nanocomposite is favorable in terms of the degradation of organic dye pollutants in comparison with the LaFeO₃ and LaFeO_{3-x}N_x photocatalysts. To check the stability of SnO₂/LaFeO_{3-x}N_x photocatalyst for RhB-dye degradation, we carried out photocatalytic stability and recyclability tests under visible-light irradiation for four consecutive recycles (each lasting 3 h). As seen in Figure 5B, the photocatalyst does not show any apparent loss in the activity even after a 12-hour irradiation period. This demonstrates that the SnO₂/LaFeO_{3-x}N_x photocatalyst is very stable and does not photocorrode during the photocatalytic reaction. To confirm which radical species is involved in the reaction process, we carried out scavengers trapping experiments in the presence of Isopropyl-alcohol (IPA, •OH scavenger), Benzo-quinone (BQ, O₂^{•-} scavenger), and EDTA-2Na (h⁺, scavenger) [36]. Appropriate amounts of each scavenger (1 mM stock) was added to the RhB-dye solution before adding the catalyst and stirred for 15 min. After catalyst addition, the sample was illuminated under visible light for 2 h. Figure 5C shows that the degradation of RhB-dye over SnO₂/LaFeO_{3-x}N_x photocatalyst is slightly suppressed in the presence of EDTA-2Na and IPA scavengers while sturdily inhibited in the presence of BQ scavenger. This reveals that the O₂^{•-} radical is the predominant active species involved in the degradation of RhB-dye over SnO₂/LaFeO_{3-x}N_x photocatalyst, and the role of h⁺ and •OH is less significant.

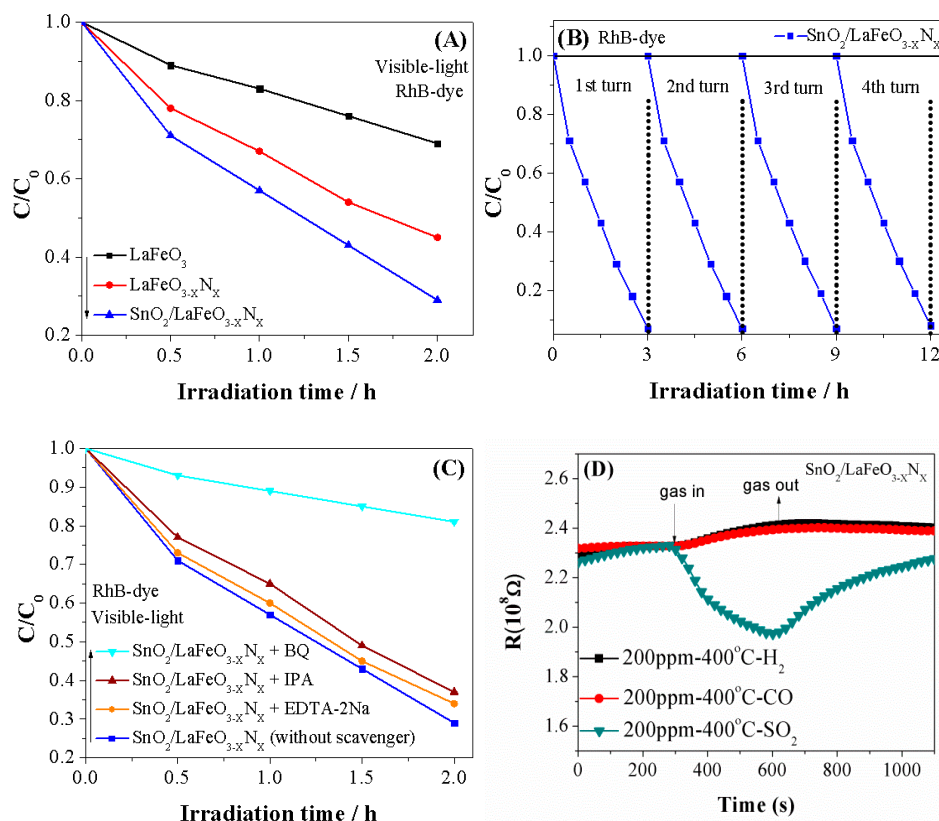


Figure 5. Photocatalytic activities for RhB-dye degradation (A) of LaFeO_3 , $\text{LaFeO}_{3-x}\text{N}_x$ and $\text{SnO}_2/\text{LaFeO}_{3-x}\text{N}_x$ photocatalysts. Photostability and recyclability test (B) and scavengers trapping experiments for RhB dye degradation (C) of $\text{SnO}_2/\text{LaFeO}_{3-x}\text{N}_x$ photocatalyst. Gas sensing performance of $\text{SnO}_2/\text{LaFeO}_{3-x}\text{N}_x$ photocatalyst for 200 ppm of H_2 , CO , and SO_2 gases at 400°C (D).

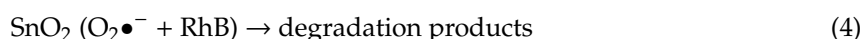
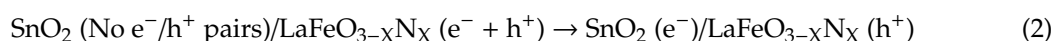
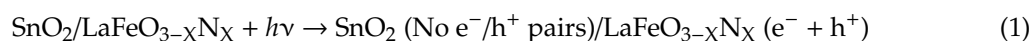
For the gas sensing activity, the sensing mechanism of n-type metal oxide semiconductors is normally associated with the space charge region formation on the oxide surfaces, owing to the electron capture on the adsorbed oxygen species [37,38]. Whenever a sensor detects a reactive gas, the gas reacts with the surface oxygen species to release electrons, which are then trapped by the adsorbed oxygen species. As a result, the conductivity of metal oxide increases. The mechanism for p-type metal oxide semiconductors is opposite. Thus, on the basis of the sensing mechanism, the main disadvantage of this type of sensor is its poor selectivity to various gases having the similar (reducing or oxidizing) nature [39,40]. However, the $\text{SnO}_2/\text{LaFeO}_{3-x}\text{N}_x$ material has different sensing behaviors to the homogeneous gases CO , H_2 , and SO_2 , as shown in Figure 5D. The resistance of the sensor material will increase when detecting CO and H_2 , but decrease when detecting SO_2 . SO_2 commonly presents similar gas sensing behavior with CO and H_2 when adsorbed on the surface of metal oxide sensing materials. However, it presented an opposite behavior here, which may contribute to the corrosive effect of SO_2 . The SO_2 adsorbed on the surface of the sensing materials to form the adsorption species SO_3 [41], which may cause a change of composition of the sensing material surface. Thus, the sensing behavior and type conductivity may transfer from p-type to n-type dominated. This indicates that the $\text{SnO}_2/\text{LaFeO}_{3-x}\text{N}_x$ material may be a promising candidate for applications in solving the poor selectivity of these types of sensors to SO_2 .

Table 1. Comparison of the RhB degradation activity of our photocatalyst with previous reports.

S. #	Photocatalyst	Light Source	RhB Degradation (%)	References
1	β -FeSe/g-C ₃ N ₄	300 W Xe-lamp	45 % (3 h)	[42]
2	R40-BiFeO _{3-x}	300 W Xe-lamp	60 % (6 h)	[43]
3	g-C ₃ N ₄ /SAPO-5	300 W Xe-lamp	47.15 % (2.5 h)	[44]
4	Bi ₂ Ti ₂ O ₇ /TiO ₂	150 W Xe-lamp	90 % (6 h)	[45]
5	SnO ₂ /LaFeO _{3-x} N _x	300 W Xe-lamp	71 % (2 h)	This work

3.4. Discussion

According to the above results, it has been demonstrated that the activity of LaFeO₃ photocatalyst for RhB-dye degradation can be greatly improved by doping N and then coupling SnO₂. This is a result of the newly formed surface states near the valence band top that effectively traps the photogenerated holes and allows the energetic electrons to transfer to the conduction band of SnO₂. To understand the charge transfer mechanism in the fabricated SnO₂/LaFeO_{3-x}N_x composite, we proposed an energy level diagram, as shown in Figure 6. As confirmed by the UV-Visible DRS spectra, the energy band gap of LaFeO₃ photocatalyst is 2.0 eV, corresponding to the light absorption of $\lambda \leq 620$ nm according to the energy band gap equation $E_g = 1240/\lambda$ where “E_g” is the energy band gap (eV) and “λ” is the wavelength (nm) of absorbed photons. From the valence band XPS spectra, as seen in Figure 3E inset, the valence band level of LaFeO₃ photocatalyst stands at 2.2 eV. After doping N, its band gap is reduced to 1.84 eV through a shift of the valence band upward to 2.04 eV which corresponds to the light absorption of approximately $\lambda \leq 674$ nm. On the other hand, the energy band gap of SnO₂ is 3.5 eV with its valence and conduction bands located at 3.54 and 0.04 eV, respectively. Thus, SnO₂ can only be excited under UV-light ($\lambda \leq 354$ nm). It is recommended that the photogenerated electrons of LaFeO₃ and LaFeO_{3-x}N_x could be relaxed to their conduction band bottom in a small time scale with energy loss, resulting in the poor charge carrier’s separation and low photocatalytic performance. However, when a heterojunction is formed between SnO₂ and LaFeO_{3-x}N_x photocatalysts and the composite is excited under visible-light, the generated highly energetic electrons of LaFeO_{3-x}N_x would transfer to the conduction band of SnO₂, leaving the excited holes in its valence band. The electrons in the conduction band of SnO₂ would probably react with the surface-adsorbed O₂ to generate superoxide radicals (O₂^{•-}) that will continue the oxidation of RhB-dye pollutant. On the other hand, the holes left in the valence band of LaFeO_{3-x}N_x would react with the surface adsorbed water and/or OH⁻ species to produce •OH radicals and then to evolve O₂. Thus, the produced active intermediates would take part in the organic pollutants degradation. In this way, the photogenerated charge carrier’s separation will significantly improve. Via this phenomenon, it is simple to make the photocatalytic activity of composite photocatalysts more practical. The fabricated visible-light-responsive nanocomposite can be utilized for effective environmental remediation. The probable stepwise reactions involved in the photocatalytic degradation of RhB over SnO₂/LaFeO_{3-x}N_x composite are described in Equations (1) to (5).



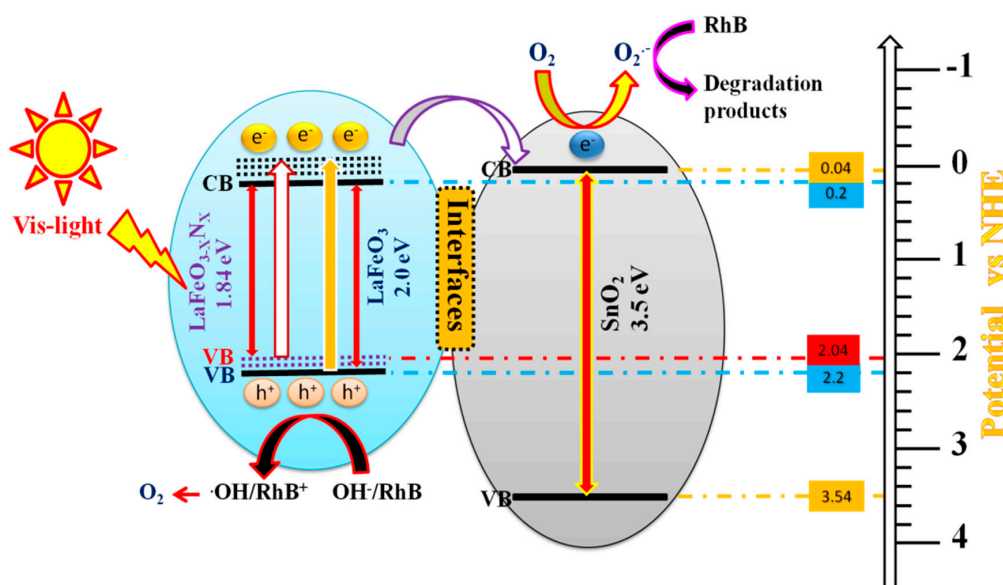


Figure 6. Schematic of the energy band gaps, charge carrier's transfer and separation, and the photocatalytic processes over $\text{SnO}_2/\text{LaFeO}_{3-x}\text{N}_x$ photocatalyst under visible-light irradiation.

4. Conclusions

$\text{SnO}_2/\text{LaFeO}_{3-x}\text{N}_x$ nanocomposite was fabricated via a wet chemical route that exhibited superior visible-light activity for RhB-dye degradation in comparison with the $\text{LaFeO}_{3-x}\text{N}_x$ and LaFeO_3 photocatalysts. This is attributable to the extended optical absorption and enhanced photo-induced charge carrier's separation via N-introduced surface states and the coupled SnO_2 . This work will trigger reasonable routes for the fabrication of highly efficient visible-light photocatalysts for effective environmental remediation. In addition, the $\text{SnO}_2/\text{LaFeO}_{3-x}\text{N}_x$ material would be a promising candidate for applications in solving the poor selectivity of this type of sensors.

Author Contributions: Conceptualization, F.-Y.W. and J.L.; Data curation, X.-T.Y. and D.D.; Formal analysis, X.-T.Y., D.D. and F.-Y.W.; Funding acquisition, X.-T.Y., F.-Y.W. and J.L.; Investigation, F.-Y.W. and J.L.; Resources, J.L.; Supervision, J.L.; Visualization, F.-Y.W.; Writing—original draft, X.-T.Y.

Funding: The financial support provided by the National Natural Science Foundation of China (Grant Nos. 51774180, 51874169, 51634004), Natural Science Foundation of Liaoning Province (Grant No. 20180550802) and Basic Scientific Research Project of colleges and universities in Liaoning Province (Grant No. 2017LNQN18).

Conflicts of Interest: The authors declare no conflict of interest.

References

- Gangu, K.K.; Maddila, S.; Jonnalagadda, S.B. A review on novel composites of MWCNTs mediated semiconducting materials as photocatalysts in water treatment. *Sci. Total Environ.* **2019**, *646*, 1398–1412. [[CrossRef](#)] [[PubMed](#)]
- Yin, X.-T.; Zhou, W.-D.; Li, J.; Wang, Q.; Wu, F.-Y.; Dastan, D.; Wang, D.; Garmestani, H.; Wang, X.-M.; Talu, S. A highly sensitivity and selectivity Pt- SnO_2 nanoparticles for sensing applications at extremely low level hydrogen gas detection. *J. Alloy. Compd.* **2019**, *805*, 229–236. [[CrossRef](#)]
- Dastan, D.; Chaure, N.; Kartha, M. Surfactants assisted solvothermal derived titania nanoparticles: Synthesis and simulation. *J. Mater. Sci. Mater. Electron.* **2017**, *28*, 7784–7796. [[CrossRef](#)]
- Yin, X.-T.; Tao, L. Fabrication and gas sensing properties of Au-loaded SnO_2 composite nanoparticles for low concentration hydrogen. *J. Alloy. Compd.* **2017**, *727*, 254–259. [[CrossRef](#)]
- Khan, M.M.; Adil, S.F.; Al-Mayouf, A. Metal oxides as photocatalysts. *J. Saudi Chem. Soc.* **2015**, *19*, 462–464. [[CrossRef](#)]
- Yin, X.-T.; Tao, L.; Wang, G.-C.; Zhou, Q.; He, W.; Wang, Q. Effects of oxygen and carbon monoxide species on the gas sensing properties of SnO_2 nanoparticles. *J. Nanoelectron. Optoelectron.* **2017**, *12*, 748–751. [[CrossRef](#)]

7. Wei, K.; Zhao, S.; Zhang, W.; Zhong, X.; Li, T.; Cui, B.; Gao, S.; Wei, D.; Shen, Y. Controllable Synthesis of Zn-Doped α -Fe₂O₃ Nanowires for H₂S Sensing. *Nanomaterials* **2019**, *9*, 994. [[CrossRef](#)] [[PubMed](#)]
8. Ge, J.L.; Zhang, Y.F.; Heo, Y.J.; Park, S.J. Advanced design and synthesis of composite photocatalysts for the remediation of wastewater: A review. *Catalysts* **2019**, *9*, 122. [[CrossRef](#)]
9. Zhou, Q.; Xu, L.; Umar, A.; Chen, W.; Kumar, R. Highly sensitive carbon monoxide (CO) gas sensors based on Ni and Zn doped SnO₂ nanomaterials. *Sens. Actuators B Chem.* **2018**, *256*, 656–664. [[CrossRef](#)]
10. Dastan, D. Effect of preparation methods on the properties of titania nanoparticles: Solvothermal versus sol-gel. *Appl. Phys. A* **2017**, *123*, 1–13. [[CrossRef](#)]
11. Yin, X.-T.; Zhou, W.-D.; Li, J.; Lv, P.; Wang, Q.; Wang, D.; Wu, F.-Y.; Dastan, D.; Garmestani, H.; Shi, Z.-C.; et al. Tin dioxide nanoparticles with high sensitivity and selectivity for gas sensors at sub-ppm level of hydrogen gas detection. *J. Mater. Sci. Mater. Electron.* **2019**. [[CrossRef](#)]
12. Nikolaou, P.; Vassilakopoulou, A.; Papadatos, D.; Topoglidis, E.; Koutselas, I. A chemical sensor for CBr₄ based on quasi-2D and 3D hybrid organic–inorganic perovskites immobilized on TiO₂ films. *Mater. Chem. Front.* **2018**, *2*, 730–740. [[CrossRef](#)]
13. Ismael, M.; Wark, M. Perovskite-type LaFeO₃: Photoelectrochemical properties and photocatalytic degradation of organic pollutants under visible light irradiation. *Catalysts* **2019**, *9*, 342. [[CrossRef](#)]
14. Peng, K.; Fu, L.J.; Yang, H.; Ouyang, J. Perovskite LaFeO₃/montmorillonite nanocomposites: Synthesis, interface characteristics and enhanced photocatalytic activity. *Sci. Rep.* **2016**, *6*, 19723. [[CrossRef](#)]
15. Wu, Y.; Wang, H.; Tu, W.G.; Liu, Y.; Tan, Y.Z.; Yuan, X.Z.; Chew, J.W. Quasi-polymeric construction of stable perovskite-type LaFeO₃/g-C₃N₄ heterostructured photocatalyst for improved Z-scheme photocatalytic activity via solid p-n heterojunction interfacial effect. *J. Hazard. Mater.* **2018**, *347*, 412–422. [[CrossRef](#)]
16. Díez-García, M.I.; Gímez, R. Metal doping to enhance the photoelectrochemical behavior of LaFeO₃ photocathodes. *ChemSusChem* **2017**, *10*, 2457–2463. [[CrossRef](#)]
17. Shin, T.H.; Ida, S.; Ishihara, T. Doped CeO₂–LaFeO₃ composite oxide as an active anode for direct hydrocarbon-type solid oxide fuel cells. *J. Am. Chem. Soc.* **2011**, *133*, 19399–19407. [[CrossRef](#)]
18. Dacquin, J.P.; Lancelot, C.; Dujardin, C.; Cordier-Robert, C.; Granger, P. Support-induced effects of LaFeO₃ perovskite on the catalytic performances of supported Pt catalysts in DeNO_x applications. *J. Phys. Chem. C* **2011**, *115*, 1911–1921. [[CrossRef](#)]
19. Zhang, L.; Xu, T.H.; Guo, Q.Y.; Ling, Z.; Zou, R.J.; Wu, Q. Enhanced photocatalytic efficiencies over A- or B-sites substituted LaFeO₃/silica fiber composites. *J. Phys. Chem. Sol.* **2017**, *110*, 136–144. [[CrossRef](#)]
20. Xu, K.; Feng, J. Superior photocatalytic performance of LaFeO₃/g-C₃N₄ heterojunction nanocomposites under visible light irradiation. *RSC Adv.* **2017**, *7*, 45369–45376. [[CrossRef](#)]
21. Armstrong, E.N.; Striker, T.; Ramaswamy, V.; Ruud, J.A.; Wachsman, E.D. NO_x adsorption behavior of LaFeO₃ and LaMnO_{3+δ} and its influence on potentiometric sensor response. *Sens. Actuators B* **2011**, *158*, 159–170. [[CrossRef](#)]
22. Toan, N.N.; Saukko, S.; Lantto, V. Gas sensing with semiconducting perovskite oxide LaFeO₃. *Physica B* **2003**, *327*, 279–282. [[CrossRef](#)]
23. Wang, Y.X.; Sun, H.Q.; Ang, H.M.; Tade, M.O.; Wang, S.B. 3D-hierarchically structured MnO₂ for catalytic oxidation of phenol solutions by activation of peroxy monosulfate: Structure dependence and mechanism. *Appl. Catal. B Environ.* **2015**, *164*, 159–167. [[CrossRef](#)]
24. Gao, X.M.; Shang, Y.Y.; Gao, K.L.; Fu, F. Plasmon sensitized heterojunction 2D ultrathin Ag/AgI-δ-Bi₂O₃ for enhanced photocatalytic nitrogen fixation. *Nanomaterials* **2019**, *9*, 781. [[CrossRef](#)]
25. Li, F.; Liu, Y.; Liu, R.; Sun, Z.; Zhao, D.; Kou, C. Preparation of Ca-doped LaFeO₃ nanopowders in a reverse microemulsion and their visible light photocatalytic activity. *Mater. Lett.* **2010**, *64*, 223–225. [[CrossRef](#)]
26. Saddat, M.; Kakhki, E.; Yavari, Z.; Saffari, J.; Ali, S.; Kakhki, E. Perovskite-type LaFeO₃ and LaFeO₃-CNTs nanocrystals as active anode for methanol oxidation in alkaline solutions. *J. Electr. Eng.* **2016**, *4*, 88–99.
27. Pasinski, D.; Zych, E.; Sokolnicki, J. The effect of N³⁻ substitution for O²⁻ on optical properties of YAG:Ce³⁺ phosphor. *J. Alloy. Compd.* **2016**, *668*, 194–199. [[CrossRef](#)]
28. Velichkova, M.M.; Lazarova, T.; Tumbalev, V.; Ivanov, G.; Kovacheva, D.; Stefanov, P.A. Naydenov, Complete oxidation of hydrocarbons on YFeO₃ and LaFeO₃ catalysts. *Chem. Eng. J.* **2013**, *231*, 236–244. [[CrossRef](#)]
29. Faye, J.; Baylet, A.; Trentesaux, M.; Royer, S.; Dumeignil, F.; Duprez, D.; Valange, S.; Tatibouet, J. Influence of lanthanum stoichiometry in La_{1-x}FeO_{3-δ} perovskites on their structure and catalytic performance in CH₄ total oxidation. *Appl. Catal. B Environ.* **2012**, *126*, 134–143. [[CrossRef](#)]

30. Thirumalairajan, S.; Girija, K.; Mastelaro, V.R.; Ponpandian, N. Photocatalytic degradation of organic dyes under visible light irradiation by floral-like LaFeO₃ nanostructures comprised of nanosheet petals. *New J. Chem.* **2014**, *38*, 5480–5490. [[CrossRef](#)]
31. Sathish, M.; Viswanathan, B.; Viswanath, R.P.; Gopinath, C.S. Synthesis, Characterization, Electronic Structure, and Photocatalytic Activity of Nitrogen-Doped TiO₂ Nanocatalyst. *Chem. Mater.* **2005**, *17*, 6349–6353. [[CrossRef](#)]
32. Chen, X.; Burda, C. Photoelectron Spectroscopic Investigation of Nitrogen-Doped Titania Nanoparticles. *J. Phys. Chem. B* **2004**, *108*, 15446–15449. [[CrossRef](#)]
33. Liang, Y.; Fang, B. Hydrothermal synthesis of SnO₂ nanorods: Morphology dependence, growth mechanism and surface properties. *Mater. Res. Bull.* **2013**, *48*, 4118–4124. [[CrossRef](#)]
34. Yang, J.; Hu, R.S.; Meng, W.W.; Du, Y.F. A novel p-LaFeO₃/n-Ag₃PO₄ heterojunction photocatalyst for phenol degradation under visible light irradiation. *Chem. Commun.* **2016**, *52*, 2620–2623. [[CrossRef](#)]
35. Attri, P.; Kim, Y.H.; Park, D.H.; Park, J.H.; Hong, Y.J.; Uhm, H.S.; Kim, K.-N.; Fridman, A.; Choi, E.H. Generation mechanism of hydroxyl radical species and its lifetime prediction during the plasma-initiated ultraviolet (UV) photolysis. *Sci. Rep.* **2015**, *5*, 9332. [[CrossRef](#)]
36. Zheng, X.K.; Yuan, J.J.; Shen, J.; Liang, J.X.; Che, J.F.; Tang, B.; He, G.Y.; Chen, H.Q. A carnation-like rGO/Bi₂O₂CO₃/BiOCl composite: Efficient photocatalyst for the degradation of ciprofloxacin. *J. Mater. Sci. Mater. Electron.* **2019**, *30*, 5986–5994. [[CrossRef](#)]
37. Yin, X.-T.; Guo, X.-M. Sensitivity and selectivity of (Au, Pt, Pd)-loaded and (In, Fe)-doped SnO₂ sensors for H₂ and CO detection. *J. Mater. Sci. Mater. Electron.* **2014**, *25*, 4960–4966. [[CrossRef](#)]
38. Zhou, Q.; Xu, L.N.; Umar, A.; Chen, W.G.; Kumar, R. Pt nanoparticles decorated SnO₂ nanoneedles for efficient CO gas Sensing Applications. *Sens. Actuators B* **2018**, *256*, 656–664. [[CrossRef](#)]
39. Katsuki, A.; Fukui, K. H₂ selective gas sensor based on SnO₂. *Sens. Actuators B* **1998**, *52*, 30–37. [[CrossRef](#)]
40. Yin, X.-T.; Lv, P.; Li, J. Study on simultaneous detection of CO and H₂ with (Pd, Fe)-modified SnO₂ and Pt-loaded SnO₂ sensors. *J. Mater. Sci. Mater. Electron.* **2018**, *29*, 18935–18940. [[CrossRef](#)]
41. Shimizu, Y.; Matsunaga, N.; Hyodo, T.; Egashira, M. Improvement of SO₂ sensing properties of WO₃ by noble metal loading. *Sens. Actuators B* **2001**, *77*, 35–40. [[CrossRef](#)]
42. Shen, S.; Zhong, W.; Wang, Z.G.; Lin, Z.; Feng, S. β-FeSe nanorods composited g-C₃N₄ with enhanced photocatalytic efficiency. *R. Soc. Open Sci.* **2019**, *6*, 181886. [[CrossRef](#)]
43. Di, L.; Yang, H.; Xian, T.; Chen, X. Enhanced photocatalytic activity of NaBH₄ reduced BiFeO₃ nanoparticles for rhodamine B decolorization. *Materials* **2017**, *10*, 1118. [[CrossRef](#)]
44. Qiu, L.; Zhou, Z.; Qiu, X.; Duo, S. Synthesis and photocatalytic degradation performance of g-C₃N₄/CQDs/SAPO-5 ternary composite. *Key Eng. Mater.* **2018**, *768*, 201–205. [[CrossRef](#)]
45. Zhou, D.; Yang, H.; Tu, Y.; Tian, Y.; Cai, Y.; Hu, Z.; Zhu, X. In situ fabrication of Bi₂Ti₂O₇/TiO₂ heterostructure submicron fibers for enhanced photocatalytic activity. *Nanoscale Res. Lett.* **2016**, *11*, 193. [[CrossRef](#)]

